Nano Research

ISSN 1998-0124 CN 11-5974/O4
https://doi.org/10.1007/s12274-019-2494-5

Research Article

Comprehensive study of a versatile polyol synthesis approach for cathode materials for Li-ion batteries

Hyeseung Chung[1], Antonin Grenier[2], Ricky Huang[1], Xuefeng Wang[1], Zachary Lebens-Higgins[3], Jean-Marie Doux[1], Shawn Sallis[4], Chengyu Song[5], Peter Ercius[5], Karena Chapman[2], Louis F. J. Piper[3], Hyung-Man Cho[1], Minghao Zhang[1] (✉), and Ying Shirley Meng[1] (✉)

[1] *Department of NanoEngineering, University of California, San Diego, La Jolla, CA 92093, USA*
[2] *Chemistry Department, Stony Brook University, Stony Brook, NY 11794, USA*
[3] *Department of Physics, Applied Physics and Astronomy, Binghamton University, Binghamton, NY 13902, USA*
[4] *Advanced Light Source, Lawrence Berkeley National Laboratory, 1 Cyclotron Road, Berkeley, CA 94720, USA*
[5] *National Center for Electron Microscopy, Molecular Foundry, Lawrence Berkeley National Laboratory, Berkeley, CA 94720, USA*

Received: 28 June 2019 / **Revised:** 25 July 2019 / **Accepted:** 26 July 2019

ABSTRACT

This work reports a comprehensive study of a novel polyol method that can successfully synthesize layered $LiNi_{0.4}Mn_{0.4}Co_{0.2}O_2$, spinel $LiNi_{0.5}Mn_{1.5}O_4$, and olivine $LiCoPO_4$ cathode materials. When properly designed, polyol method offers many advantages such as low cost, ease of use, and proven scalability for industrial applications. Most importantly, the unique properties of polyol solvent allow for greater morphology control as shown by all the resulting materials exhibiting monodispersed nanoparticles morphology. This morphology contributes to improved lithium ion transport due to short diffusion lengths. Polyol-synthesized $LiNi_{0.4}Mn_{0.4}Co_{0.2}O_2$ delivers a reversible capacity of 101 and 82 $mAh \cdot g^{-1}$ using high current rate of 5C and 10C, respectively. It also displays surprisingly high surface structure stability after charge–discharge processes. Each step of the reaction was investigated to understand the underlying polyol synthesis mechanism. A combination of *in situ* and *ex situ* studies reveal the structural and chemical transformation of Ni-Co alloy nanocrystals overwrapped by a Mn- and Li-embedded organic matrix to a series of intermediate phases, and then eventually to the desired layered oxide phase with a homogeneous distribution of Ni, Co, and Mn. We envisage that this type of analysis will promote the development of optimized synthesis protocols by establishing links between experimental factors and important structural and chemical properties of the desired product. The insights can open a new direction of research to synthesize high-performance intercalation compounds by allowing unprecedented control of intermediate phases using experimental parameters.

KEYWORDS

polyol, cathode, synthesis, nanoparticle, $LiNi_{0.4}Mn_{0.4}Co_{0.2}O_2$ (NMC)

1 Introduction

One of the most pressing challenges that modern society faces is to provide energy sources for a variety of applications, ranging from small portable devices to electric vehicles (EVs) and large grid-scale systems to store energy from intermittent solar or wind-driven devices [1]. Recently, enough technological advancement has been made that Li-ion batteries (LIBs) are now considered the most promising solution for this problem. There is, however, no single universal battery material that can meet the demands of all these applications. Just as there are various devices that can benefit from Li-ion battery technology, each respective application has a different set of prioritized features for energy storage, such as high power for power tools, high energy for portable devices, or competitive cost for grid-scale energy storage [2–4]. Particularly, cathode materials have received considerable attention because they are considered as the primary determinant for meeting these demands. As a result, diverse cathode materials have been proposed and intensely investigated by both academia and industry [5]. Categorized by their unique crystal structures, the current state-of-the-art cathode materials include layered oxide compounds ($LiCoO_2$, $LiNi_xMn_yCo_{1-x-y}O_2$, $LiNi_{0.85}Co_{0.10}Al_{0.05}O_2$), spinel compounds ($LiMn_2O_4$, $LiNi_{0.5}Mn_{1.5}O_4$ (LNMO)), and olivine compounds ($LiFePO_4$, $LiCoPO_4$ (LCP)).

The evaluation of these cathode materials cannot be conducted without the exploration of diverse synthetic methods. To date, the synthesis process to make the cathode oxide material has been developed with the goal of producing a product of a specific phase, with a desired particle size and shape, and without local compositional and crystallographic inhomogeneities [6]. Many developed methods proved to have advantages but were simultaneously accompanied by some major drawbacks. In the traditional solid-state method, the mixing of multiple metal sources is done by manual grinding or ball milling. This method is simple and easy in preparation but results in a microcrystalline product with long lithium ion diffusion pathways as well as inhomogeneous morphology and metal distribution. Such features have an adverse effect on the electrochemical reaction kinetics. The co-precipitation method compensates for some of these shortcomings, but it also requires a careful control of pH when using carbonate [7, 8] or an inert atmosphere to minimize the undesired impurities when using hydroxide [9]. Previous studies show that the hydrothermal method is an effective way to synthesize cathode materials with high crystallinity, but its complex set up and

Address correspondence to Ying Shirley Meng, shirleymeng@ucsd.edu; Minghao Zhang, miz016@eng.ucsd.edu

high cost make it impractical to be applied in large-scale synthesis [10, 11]. The sol-gel method also poses challenges due to the high pH sensitivity of the gel formation. An inappropriate control of the pH may result in the formation of a precipitate instead of a gel, producing undesirable inhomogeneity of the product [12]. Lastly, most of the conventional synthetic methods fall short on versatility, making systematic evaluation of cathode materials extremely challenging. Different synthetic factors must be taken into consideration each time a cathode material is made by a different method.

Herein, we developed a novel polyol-mediated synthesis process that is versatile enough to prepare three cathode materials with layered, spinel, and olivine crystal structures. Developed by Fievet and co-workers in the 1980s, polyol synthesis has been widely used in recent decades, but its scope has been mostly limited to the synthesis of simple metals and metal oxides [13, 14]. In this method, the polyol medium acts as a chelating agent, a solvent, and a reducing agent, guaranteeing a stable dispersion of nanoparticles with controlled size distribution [15]. In this work, our group has extended this synthesis method to develop more complex metal oxides used as cathode materials in batteries. Polyol synthesis yields completely dispersed cathode nanoparticles with a narrow particle size distribution and competitive electrochemical performance. With the growing interest for solid state lithium batteries, cathode materials with dispersive morphology are strongly desirable as they can provide more intimate solid–solid contact. Using a combination of powder X-ray diffraction (XRD), high-angle annular dark-field scanning transmission electron microscopy (HAADF-STEM), and energy dispersive spectroscopy (EDS), we confirmed high crystallinity and uniform elemental distribution for all three polyol-synthesized cathode materials. Finally, HAADF-STEM images and electron energy loss spectroscopy (EELS) for cycled $LiNi_{0.4}Mn_{0.4}Co_{0.2}O_2$ (NMC) material were collected to confirm its structural stability after charge–discharge cycling processes.

Based on the results of these three polyol-synthesized cathode materials, we believe that the polyol method can provide a valuable platform for evaluating high-performance, nano-dispersed cathode materials for LIBs. Furthermore, using a combination of *in situ* and *ex situ* characterizations, we have constructed a comprehensive picture of how the reaction progresses during each step of the synthesis. In the case of layered NMC, polyol-mediated solution yields a core/shell structure with Ni-Co alloy nanocrystals surrounded by Mn- and Li-embedded organic matrix. Using *in situ* XRD, the progression of intermediate phases during the post heat treatment was analyzed with respect to the temperature. The detailed knowledge of the reaction mechanism will help to efficiently provide feedback to researchers, such as controlling reaction temperature or heating rate, to eventually find the most optimized synthetic conditions for polyol process.

2 Experimental

2.1 Synthesis

Synthesis for cathode nanoparticles is a two-step process which involves: 1) preparation of the precursors via polyol solution reaction and 2) heat-treatment to complete the phase transformation and eliminate impurities.

2.1.1 *$LiNi_{0.4}Mn_{0.4}Co_{0.2}O_2$ nanoparticles*

Transition metal acetates—$Ni(CH_3COO)_2{\cdot}4H_2O$ (0.012 mol), $Mn(CH_3COO)_2{\cdot}4H_2O$ (0.012 mol), and $Co(CH_3COO)_2{\cdot}4H_2O$ (0.006 mol)—and $LiOH{\cdot}H_2O$ (0.0345 mol) were mixed in 80 mL of triethylene glycol along with citric acid (0.045 mol). The mixture was heated at 230 °C with constant stirring for 3 h in a round bottom flask connected to a reflux. The resulting solution was washed with ethanol several times with a centrifuge and subsequently dried at 80 °C overnight. As-obtained precursors were decomposed at 450 °C for 12 h and then annealed as a pellet for 5 h at 850 °C in air.

2.1.2 *$LiNi_{0.5}Mn_{1.5}O_4$ nanoparticles*

$LiNi_{0.5}Mn_{1.5}O_4$ was synthesized with stoichiometric ratio of $Ni(CH_3COO)_2{\cdot}4H_2O$ (0.0075 mol), $Mn(CH_3COO)_2{\cdot}4H_2O$ (0.0225 mol), and $LiOH{\cdot}H_2O$ (0.015 mol) in 100 mL of tetraethylene glycol and citric acid (0.030 mol). The mixture was heated at 230 °C with constant stirring for 3 h. The precipitate was washed with ethanol and subsequently dried at 80 °C for overnight. As-obtained precursors were decomposed at 450 °C for 12 h and then annealed as a pellet for 1 h at 800 °C in air.

2.1.3 *$LiCoPO_4$ nanoparticles*

LiH_2PO_4 (0.015 mol) and $Co(CH_3COO)_2{\cdot}4H_2O$ (0.015 mol) were added as stoichiometric ratio in 100 mL of tetraethylene glycol along with 0.030 mol of polyvinylpyrrolidone (M_W = 58,000). The mixture was heated at 270 °C with constant stirring for 3 h. The precipitate was washed with ethanol and subsequently dried at 80 °C overnight. As-obtained precursors were decomposed at 450 °C for 12 h and then annealed as a pellet for 5 h at 700 °C in air.

2.2 *Ex situ* powder XRD

Powder XRD of NMC and LNMO samples were collected on a laboratory X-ray diffractometer, Bruker D8, using a Cu Kα radiation. The data was collected by continuous scanning of a detector covering an angular range from 10.0° to 80.0° with a scan rate of 0.02 °·s^{-1} with Cu Kα radiation (λ = 1.54059 Å). In the case of LCP, the data were collected on a Bruker APEX II Ultra diffractometer equipped with Mo Kα radiation (λ = 0.71073 Å) at the UCSD X-ray Crystallography Facility. Diffraction images were merged/integrated in DIFFRAC.EVA (Bruker, 2018) to produce 2d-plots.

All Rietveld refinements were conducted with a pseudo-Voigt profile using FullProf software.

2.3 Inductive coupled plasma atomic emission spectroscopy (ICP-AES)

The amount of Li and transition metal ions (Ni, Co, Mn) was analyzed by ICP-AES (Perkin Elmer Plasma 3700). The ICP-AES equipped with two monochromators covering the spectral range of 167–785 nm with a grated ruling of 3,600 lines·mm^{-1}. The system can analyze range of less than 1 part per billion.

2.4 Scanning electron microscopy (SEM)

The particle sizes and morphologies were checked using ultrahigh resonance scanning electron microscope (FEI Apreo SEM) at an acceleration voltage of 5 kV. The sample has been coated by sputtering with iridium prior to the measurement.

2.4 Brunauer–Emmett–Teller (BET)

N_2 gas physisorption analysis was performed with a Quantachrome Autosorb – iQ/MPXR surface area and porosity analyzer. Each sample was loaded into a quartz sample tube, inserted into the machine, and was degassed under vacuum at 80 °C for 8 h prior to the measurement.

2.5 Electrochemistry

For the composite electrode fabrication, the slurry consisting of 80 wt.% active materials, 10 wt.% acetylene carbon black, and 10 wt.% poly(vinylidene fluoride) (PVDF) in N-methyl pyrrolidone (NMP) was coated on an aluminum foil current collector and then dried overnight in a vacuum oven at 80 °C. As-prepared electrodes were punched, pressed uniaxially, dried again at 80 °C for 6 h and then stored in an argon-filled glovebox (H_2O level of < 1 ppm) (MBraun, Germany) before cell assembly. For the electrochemical characterizations,

lithium metal was used for the negative (counter) electrode with Celgard separator. The electrolyte was a 1 M solution of lithium hexafluorophosphate ($LiPF_6$) in a 3:7 volume mixture of ethylene carbonate (EC) and dimethyl carbonate (DMC). The cell used for the electrochemical tests was assembled in a glove box (MBraun, Germany) filled with purified argon gas. The as-prepared cell was charged and discharged in the voltage ranges of 2.5–4.3 and 2.5–4.7 V for NMC, 3.5–4.85 V for LNMO, and 2.8–4.95 V for LCP. Theoretical capacity was assumed to be 200 $mAh{\cdot}g^{-1}$ for NMC, 146.7 $mAh{\cdot}g^{-1}$ for LNMO, and 167 $mAh{\cdot}g^{-1}$ for LCP. An Arbin battery cycler was employed to carry out all the galvanostatic cycling tests.

2.6 Transmission electron microscopy (TEM)

High-resolution STEM images and EELS of pristine NMC, LNMO, and LCP and cycled NMC were carried out using the double aberration-corrected scanning TEM (TEAM 0.5) operated at an acceleration voltage of 300 kV installed at the Molecular Foundry at Lawrence Berkeley National Laboratory. All annular dark-field STEM micrographs were recorded in TEAM 0.5 with a convergence angle of 30 mrad and a probe size of < 1 Å after fine-tuning of the probe corrector at 300 kV. EDS/EELS elemental mappings and as-synthesized NMC precipitate characterizations were performed on a double aberration-corrected scanning TEM (JEOL JEM-ARM300CF) at 300 kV installed at the UC Irvine Materials Research Institute (IMRI). To minimize possible electron beam irradiation effects, all the EELS and EDS spectra presented in this work were acquired from areas without pre-beam irradiation.

2.7 Synchrotron XRD and pair distribution function (PDF) analysis

X-ray scattering data were recorded using high-energy X-rays (λ = 0.2113 Å) provided by beamline 11-ID-B at the Advanced Photon Source at Argonne National Laboratory. Powders were loaded in amorphous SiO_2 tubes and placed in the flow-cell/furnace for heating under controlled atmosphere [16]. Air (1 cc/min) was flown through the tube as temperature was increased up to 850 °C in 10 °C steps. To more closely resemble high-temperature treatment condition, another set of experiment was conducted with the pre-heated sample. This sample was heated at 450 °C for 12 h and cooled down back to room temperature. Air (4 $cc{\cdot}min^{-1}$) was flown as the temperature was increased up to 900 °C in 50 °C steps. For both sets of data, two-dimensional (2D) images were recorded in transmission geometry using an amorphous-Si detector, and integrated into one-dimensional (1D) patterns using GSAS-II [17], using CeO_2 or LaB_6 standards as calibrant. At each temperature step, data was recorded at two sample-to-detector distances to provide Q ranges suitable for XRD and atomic PDF analyses. PDFs (Q_{max} = 24 $Å^{-1}$) were calculated using PDFgetX3, and modeled using PDFgui [18, 19].

2.7.1 *Le Bail refinements*

Lattice parameters of the face-centered cubic (fcc) ($Fm\bar{3}m$) phase identified in the NMC442 precipitate and lattice parameters of the spinel intermediate ($I41/amd$) identified at 230 °C, were obtained from Le Bail refinements of the synchrotron XRD data using TOPAS Academic V6. Diffuse scattering intensity from amorphous SiO_2 tubes was fit using a series of pseudo Voigt functions and an 8-term Chebyshev-type function. The peak profile was fit using CS_L/CS_G macros defined in TOPAS.

2.7.2 *PDF refinements*

Parameters included lattice parameters, isotropic atomic displacement parameters, scale factor and spdiameter. The spdiameter parameter accounts for the decrease of the PDF amplitude with increasing r due to limited diameter of spherical scattering domains. The occupancies of Ni/Co were fixed to 1 and their relative occupancy was ignored considering their similar scattering factors. The Q_{damp} (correction for PDF dampening due to instrumental limitations) was obtained from a Ni reference. The weighted reliability factor R_w characterizes the agreement between the model and the data, with smaller value corresponding to better a fit.

2.7.3 *Rietveld refinements*

High-temperature heat treatment for 450 °C pre-heated sample was analyzed by the Rietveld method. The cell parameter refinements were carried out with a pseudo-Voigt profile using Fullprof software in the full pattern matching mode with WinPLOTR [20, 21]. From 850 °C, SiO_2 tube crystallizes, so the refinement was performed after excluding region between 3.3°–3.9°. More details can be found in Table S7 in the Electronic Supplementary Material (ESM).

2.8 Soft X-ray absorption spectroscopy (sXAS)

sXAS experiments were performed in total electron yield (TEY), total fluorescence yield (TFY) and partial fluorescence yield (PFY) modes using the iRIXS endstation at beamline 8.0.1 at the Advanced Light Source (ALS) at Lawrence Berkeley National Laboratory (LBNL) [22]. The X-ray absorption spectra were recorded in TEY mode using the sample drain current, TFY mode using a channeltron, and PFY mode using the high throughput spectrograph (htRIXS). These modes provide surface (TEY) and bulk (TFY/PFY) sensitivity. All spectra were normalized to the current from a reference Au-coated mesh in the incident photon beam. For the Mn L_3-edge, photon energies were normalized to a TiO_2 reference. For the Co and Ni L_3-edges, photon energies were normalized to a Ni-metal reference. Previously reported Mn L_3-edge spectra for MnO, Mn_2O_3, and Li_2MnO_3 are used as Mn^{2+}, Mn^{3+}, and Mn^{4+} references, respectively [23]. Metallic Ni and Co films mounted on the iRIXS manipulator were used as Ni^0 and Co^0/Co^{2+}, respectively, with the Co film having a slightly reduced Co^{2+}-like surface. Pristine commercial $LiNi_{0.8}Co_{0.15}Al_{0.05}O_2$ (NCA) powder was used as a Ni^{3+} and Co^{3+} reference.

3 Results and discussion

3.1 Material characterization

The synthesis process of the polyol method is schematically shown in Fig. 1(a). The precipitate is obtained after the high-temperature polyol solution reaction. The as-obtained precipitates have three distinct colors—light brown (NMC precursor), greyish brown (LNMO precursor), and light purple (LCP precursor)—due to different compositions. Afterwards, all precipitates go through a two-step heat treatment process. The polyol medium acts as a low solubility solvent, chelating agent, and stabilizing agent at the same time during the reaction [24]. Such conditions are favorable to control the nucleation and growth of the synthesized particles. As a result, the SEM micrographs show that all three polyol-synthesized cathodes have highly dispersed nanoparticles with narrow size distribution (Figs. 1(b)–1(d)). Dispersive nanoparticles are ideal for any surface-interface study, since there is no micron-sized meso-structure morphology present in the sample. Such morphology confirms that polyol synthesis method has a potential to provide an excellent synthetic platform for various fundamental studies on cathode nanoparticles. Polyol-synthesized NMC and LNMO cathodes are highly homogeneous network of nanoparticles with 138 and 180 nm in diameter with 40.9 and 41.7 nm for standard deviations, respectively (Fig. S1 in the ESM). Polyol-synthesized LCP has slightly larger particles which are around 477 nm in diameter with wider standard deviation of 68.6 nm, but it is still absent of any secondary meso-structure. Figure S2 in the ESM clearly shows the difference in the morphology between commercial and polyol-synthesized NMC. Without a secondary meso-structure, polyol-synthesized NMC

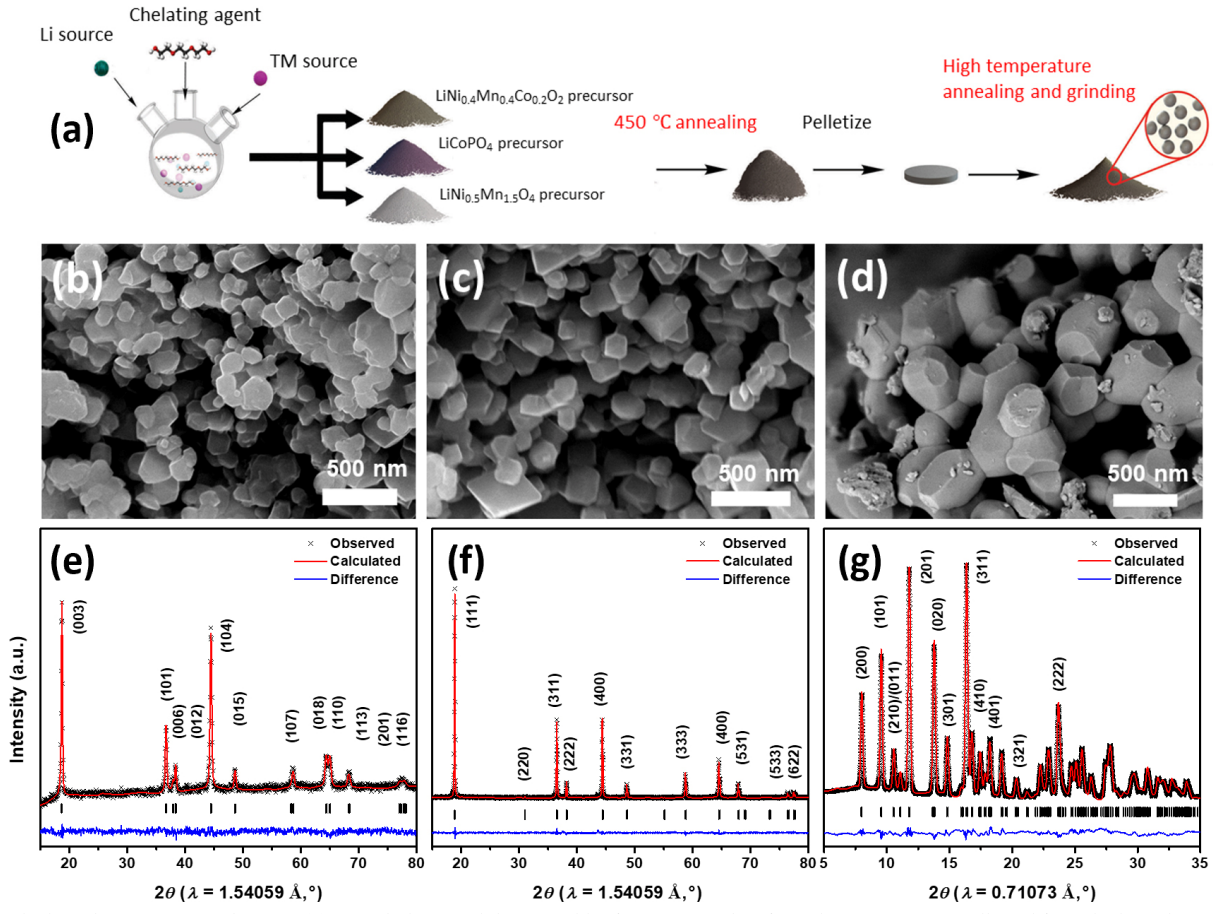

Figure 1 Polyol synthesis reaction schematic (a), morphology, and the Rietveld refinement results of powder XRD pattern collected for polyol-synthesized (b) and (e) layered NCM, (c) and (f) spinel LNMO, and (d) and (g) olivine LCP materials.

has five times more surface area (2.83 $m^2 \cdot g^{-1}$) than commercial NMC (0.5 $m^2 \cdot g^{-1}$) and possibly lower tap density. Similarly, BET measurements show that polyol-synthesized LNMO and LCP have surface areas of 4.13 and 8.13 $m^2 \cdot g^{-1}$. Indirect correlation of particle size and surface area can come from possible aggregation for polyol-synthesized NMC and LNMO as commonly observed in nanoparticle synthesis [25–27]. Small particle size increases the contact area with the electrolyte for charge transfer and shortens Li-ion diffusion length, thus enhancing the rate capability as described in a later section [28].

The XRD analyses of the synthesized NMC, LNMO, and LCP are shown in Figs. 1(e)–1(g). Rietveld refinements were performed for each sample to confirm their crystal structure. The corresponding crystallographic parameters are tabulated in Table S1 in the ESM. Results confirm pure phase of layered NMC, spinel LNMO, and olivine LCP obtained through the polyol method, as all peaks are indexed by the expected space groups with no indication of crystalline impurities. In the case of NMC, all diffraction peaks in the pattern are indexed by a rhombohedral layered phase with the $R\bar{3}m$ space group. XRD pattern of polyol-synthesized LNMO exhibits peaks characteristic of the cubic spinel phase with the $Fd\bar{3}m$ space group. As a disordered LNMO spinel material, the Li sits in the tetrahedral sites with Ni and Mn randomly occupying in 16c octahedral sites. The minimal intensity of the (220) peak indicates low occupation of transition metals in tetrahedral sites [29]. This was consistent with our Rietveld refinement value, which only shows 1.7% of cation mixing. Nickel-rich rocksalt phase is a common concomitant impurity phase present in this material after high temperature heat-treatment [30, 31], but no sign of any impurity was detected in the XRD pattern of our synthesized material, confirming the excellent purity. The short annealing time (800 °C, 1 h) minimizes Li evaporation, therefore, limits the formation of $Li_xNi_{1-x}O$ impurity [32, 33]. Lastly, XRD patterns of the synthesized LCP particles are shown in Fig. 1(g). All the diffraction peaks are indexed by the *Pnma* space group. The olivine structure is based on a distorted hexagonal close-packed oxygen array with P atoms occupying tetrahedral sites and Li and Co occupying the 4a and 4c octahedral sites, respectively [34–36].

Aberration-corrected STEM was used to directly observe the local crystal structures of NMC, LNMO, and LCP at the atomic scale. As polyol-synthesized cathodes are completely dispersed nanoparticles, no special sample preparation for STEM was needed [37]. Figure 2 shows representative HAADF-STEM images of the polyol-synthesized cathodes in the pristine state. As shown in the image of NMC (represented by the blue frame) taken along the [100] zone axis, the positions of transition metals in 3a sites are atomically resolved, which confirms a well-defined layered structure. Li (3b sites) and O (6c sites) are not visible due to their low atomic mass in Z-contrast HAADF-STEM images [38]. According to the Rietveld refinement, polyol-synthesized NMC features 6.47% of Li/Ni cation mixing. A small degree of cation mixing is also observed in the few atomic layers of the surface region in high resolution images, as previously observed in other studies [39].

Representative HAADF-STEM images of the pristine LNMO were taken along the [110] zone axis (red frame). This direction allows the position of transition metal (TM) heavy atomic columns to be identified clearly as a diamond configuration. As shown, two different transition metal columns can be assigned as TM1 and TM2. Stronger contrast is observed in TM1 than in TM2 column position, because the stacking density of the TM1 is twice to that of TM2 [40, 41]. The well-defined spinel structure in the bulk material extends to the surface. Lastly, the purple color frame in Fig. 2 shows

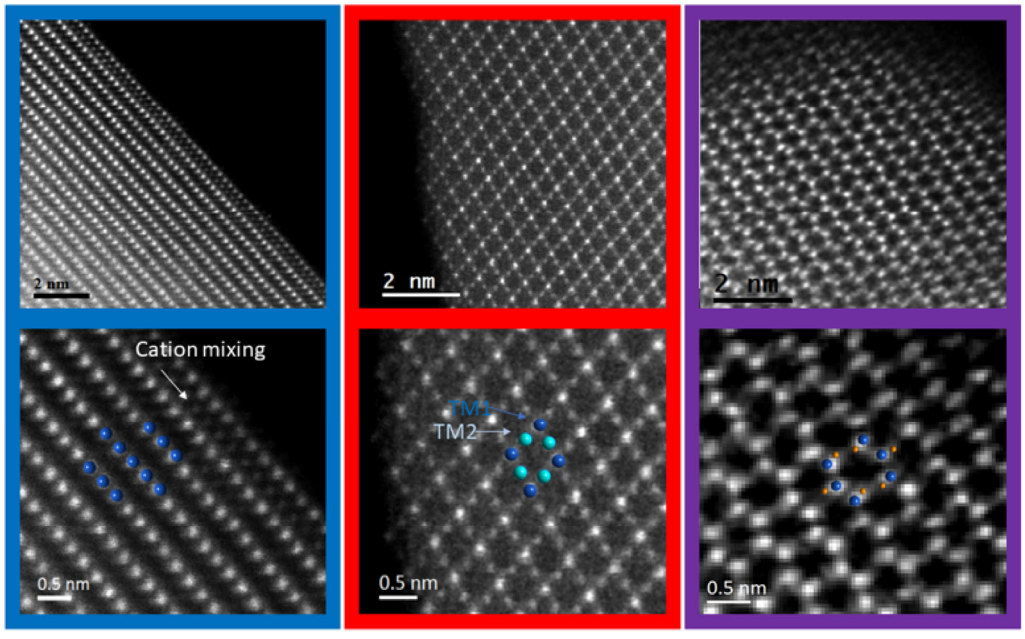

Figure 2 HAADF-STEM images of the polyol-synthesized layered NMC (blue frame), spinel LNMO (red frame), and olivine LCP (purple frame) materials. Dark and light blue color circles represent transition metal (Ni, Co, or Mn), while orange represents phosphorus ions.

synthesized LCP viewed along the [010] projection. The [010] direction has been chosen because it allows for the identification of the position of Co, P, O, and Li with separate aligned columns. Bright contrast produced by Co atoms can be clearly observed in a hexagon configuration under the HAADF-STEM mode. Because P atomic columns are adjacent to the Co site, Co and P cannot be distinctively resolved [42].

The distribution of transition metal at the atomic level is extremely important as it correlates closely with the materials' rate capability and cyclability [11, 43, 44]. Zheng et al. found that a careful choice of synthetic conditions applied for the precursor preparation can mitigate the transition metal segregation, thus enhancing the electrochemical performance of layered oxides [11]. Motivated by this study, we investigated the local chemical species in both the bulk and surface of the pristine cathode materials using energy dispersive X-ray spectroscopy in STEM. Polyol method is a one-pot synthesis method, which involves all the transition metal and lithium precursors reacting together at high temperature. As shown in Fig. S4 in the ESM, all the elements in the polyol-synthesized NMC, LNMO, and LCP are uniformly distributed, with no apparent segregation. Additionally, the stoichiometry of the polyol-synthesized NMC, LNMO, and LCP were confirmed with ICP-AES, and is close to their nominal stoichiometry, with variances in the range of experimental error. These results are presented in Table S2 in the ESM.

3.2 Electrochemical characterization

The three polyol-synthesized cathode materials were characterized by a series of electrochemical properties measured in Li half-cells. Figure 3 shows electrochemical properties and redox potentials for NMC, LNMO, and LCP. Layered NMC exhibits typical galvanostatic charge–discharge profile between 2.5 and 4.3 V with charge and discharge capacities of 158 and 140 mAh·g^{-1} respectively for C/10. The corresponding differential capacity versus voltage (dQ/dV) curves are plotted in Fig. 3(c). The broad peak between 3.7 and 4.2 V on the 1st charge is related to the oxidation of Ni ions (Ni^{2+}/Ni^{4+}) and Co ions (Co^{3+}/Co^{4+}), and the reduction peak found in similar potential indicates reversible Li insertion in the layered structure [45]. After 50 cycles, the material still maintains 87.1% of its initial capacity with 122 mAh·g^{-1}. In the case of spinel LNMO, the material was tested with C/10 between 3.5–4.85 V. Both the voltage profile and dQ/dV plot clearly show the redox couple of Mn^{3+}/Mn^{4+} (4.0 V) and Ni^{2+}/Ni^{4+} (4.6–4.8 V). The peak splitting in 4.6–4.8 V region is due to two oxidation steps: Ni^{2+}/Ni^{3+} and then Ni^{3}/Ni^{4+} [46, 47]. Spinel LNMO delivers the charge and discharge capacity of 137 and 125 mAh·g^{-1}. Even after 50 cycles, the material retained 94.4% of its capacity, showing an excellent cycling stability. Only negligible voltage decay is observed for the 1st and 50th cycles as well. Cycling retention for LNMO by polyol far exceeds the same material made by more conventional sol-gel method, which also yields dispersive morphology (Fig. S5 in the ESM). At elevated temperature (55 °C), polyol-synthesized LNMO maintained 97.7% of its first discharge capacity after 30 cycles, while sol-gel synthesized LNMO maintained only 73.0%. Lastly, olivine LCP has been tested between 2.8–4.95 V for C/10. As shown, LCP redox couples correspond to the redox of two two-phase regions, specifically $LiCoPO_4/Li_{0.66}CoPO_4$ (4.8 V) and $Li_{0.66}CoPO_4$ /$CoPO_4$ (4.9 V) vs. Li/Li^+ during the charge and two corresponding reduction peaks at 4.78 and 4.71 V. In agreement with previously published results, these two steps during charge–discharge are more pronounced at the 50th cycle than during the 1st cycle [48, 49]. Both oxidation peaks in the initial cycle are shifted to more positive potential when compared with further cycles, which indicates the slow kinetics of the initial delithiation of $LiCoPO_4$. As shown, LCP has first charge and discharge capacity 137 and 108 mAh·g^{-1}, and high charge and discharge energy density of 646 and 504 Wh·kg^{-1} due to high redox potential. LCP, unfortunately, suffers from poor cycle life, mainly attributed to the parasitic degradation reactions at the interface of the electrode and the electrolyte (Table S3 in the ESM). The working potential of LCP far exceeds the stability limit of standard carbonate-based electrolytes (~ 4.5 V) [36]. The decomposition products of the electrolyte form resistive films on the particle surfaces, which hinder lithium intercalation reaction thereafter.

Similar to spinel LNMO and olivine LCP, layered NMC can also be evaluated with a high voltage cutoff of 4.7 V. By increasing the operating voltage, polyol-synthesized NMC can reach up to 251 and 207 mAh·g^{-1} of the first cycle charge and discharge capacity. This corresponds to 1,026 and 805 Wh·kg^{-1} of energy density, which exceeds both LNMO (635/571 Wh·kg^{-1}) and LCP (646/504 Wh·kg^{-1}) materials. Additional studies were therefore performed for NMC to

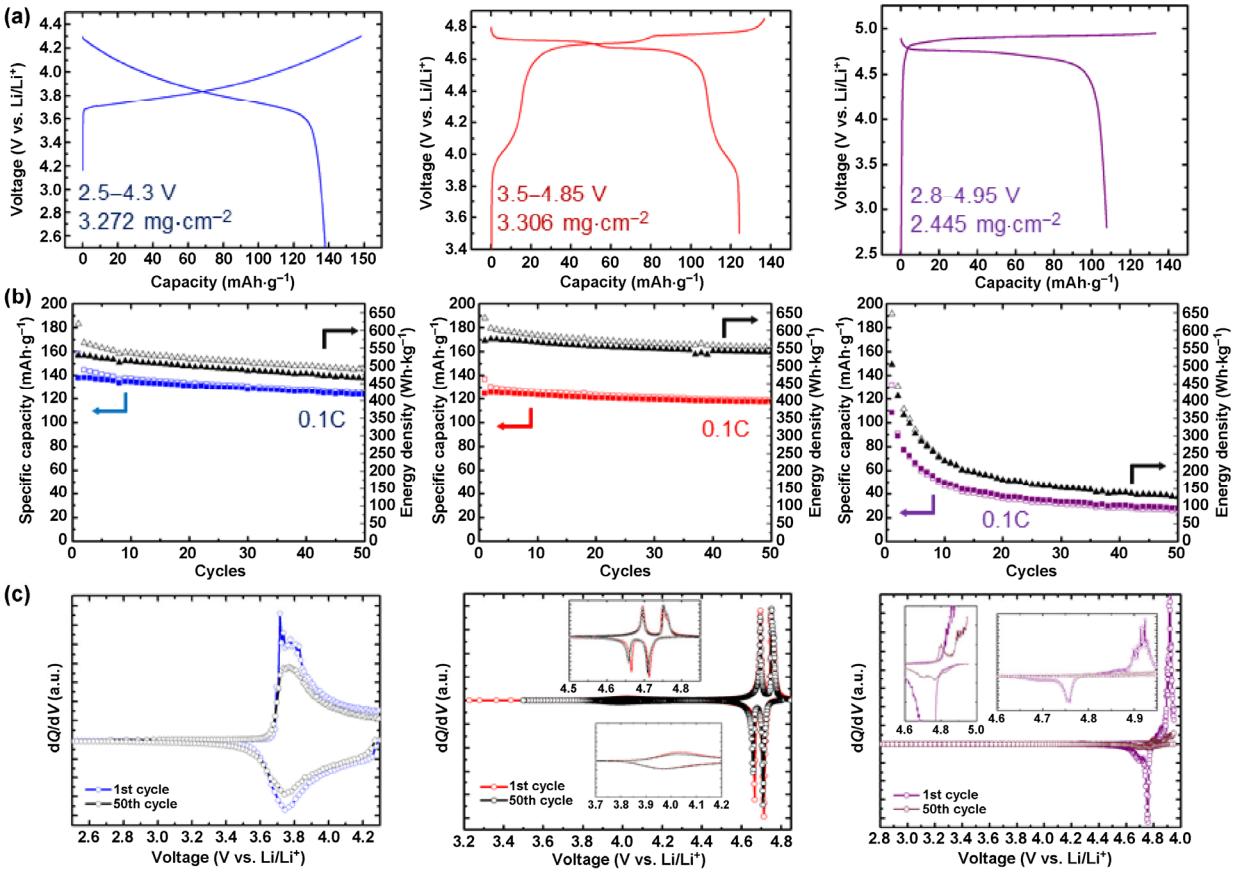

Figure 3 (a) First charge and discharge voltage profile, (b) cycling performance, and (c) dQ/dV in the voltage range of 2.5–4.3 V for NMC (blue), 3.5–4.85 V for LNMO (red), and 2.8–4.95 V for LCP (purple).

evaluate the material as a next generation storage material with high energy density.

First, we studied the effect of current density on the charge–discharge profile of polyol-synthesized NMC. To achieve high rate rechargeable batteries, many studies have focused on controlling the dimensions of the active particles [50]. Nevertheless, as mentioned earlier, reducing the size by producing nanosized particles has drawbacks as a large surface area could promote undesirable side reactions between active material and electrolyte. Consequently, it remains a great challenge to synthesize the desired nanostructured morphology to fulfill both the energy requirement and cycling stability at the same time. Previous work by Kim et al. showed that polyol synthesis of $LiFePO_4$ nanoparticles showed excellent capacity retention at high current densities with the monodispersed uniform morphology [51]. Similarly, our synthesized NMC show excellent capacity retention when charged and discharged at different current rate ranging from C/10 to 10C. To illustrate, the result shows that the discharge capacities could reach 131, 123, 101, and 82 mAh·g^{-1} for C/3, 1C, 5C, and 10C rate (Fig. S6 in the ESM). The capacity for all current densities is stable with all maintaining reversible capacity retention ratios above 87% even after 50 cycles. The electrochemical performance is superior to that reported in the literature for pristine $LiNi_{0.4}Mn_{0.4}Co_{0.2}O_2$ material tested under standard conditions, especially at high current density (Table S4 in the ESM) [52].

Additionally, we studied the effect of high voltage operation on the cyclability of NMC. Figure S7 in the ESM displays the voltage profile of NMC at high voltage operation (2.5–4.7 V) with C/10 rate. Although it initially displayed higher specific capacity, the capacity of the NMC electrode continues to decrease during cycling, while lower voltage operation (2.5–4.3 V) experiences smaller capacity fade. Previous electron microscopy studies show that this high voltage operation in NMC is accompanied by structural transformations at the particle surface from layered to spinel-like and/or rock-salt-like structures. Merely after 1-cycle at 4.7 V cutoff, Lin *et al.* observed a surface reconstructed layer from $R\bar{3}m$ to $Fm\bar{3}m$ [53]. Motivated by this observation, we have investigated the local crystal and electronic structure of the cycled sample using STEM-EELS. Interestingly, even after 10 cycles at 4.7 V cutoff, the surface structure of polyol-synthesized NMC particles remains mostly intact, showing a layered structure (Fig. 4(a)) similar to the pristine material (shown in Fig. 2). Multiple regions were analyzed to confirm the consistency of our results (Fig. S8 in the ESM). Only one out of five particles (Fig. 4(b)) showed a surface reconstruction layer for the 10-cycled sample. Furthermore, EELS was acquired to assess the bulk and surface structure changes of pristine and cycled NMC. EELS data were also collected at several positions to ensure that the results presented in Fig. 4(c) are representative of the sample studied. The pre-peak of the O K-edge is associated with the hybridization states between transition metal 3d and oxygen 2p orbitals in the octahedral unit, thus it can be correlated with the oxidation states of transition metals [53, 54]. As shown, the oxygen electronic structure is well-maintained both at the bulk and the surface of cycled NMC particles. Such results correlate well with the HAADF-STEM images, since surface reconstruction after cycling would have led to a reduction of the transition metal valence and oxygen vacancy. Shkrob et al. reported that protons from H_2O molecules can exchange with Li ions without changing the lattice symmetry of cathode materials, which leads to the capacity degradation in Li-ion batteries [55]. It is therefore possible that the absence of water during the polyol synthesis helps to prevent proton insertion into NMC structure, creating a more stable atomic structure in the pristine material that is more resistant to surface reconstruction. Instead of originating from surface reconstruction, continuous capacity degradation for polyol-synthesized NMC could mainly stem from undesirable side

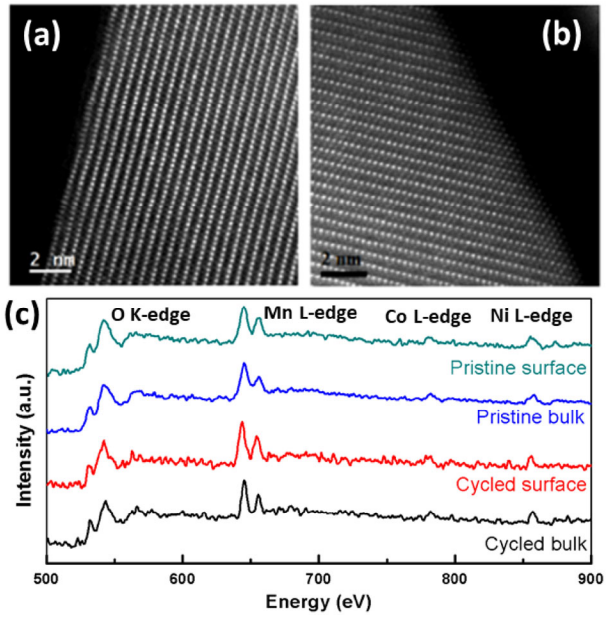

Figure 4 HAADF-STEM images (a) and (b) and EELS spectra at the surface and bulk regions (c) of NMC cathodes after 10 cycles at C/10 in the voltage range of 2.5–4.7 V. (a) and (b) represent different particles observed.

reactions with the electrolyte, aggravated by the high state-of-charge and large surface area [56]. We further explored the polyol synthesis mechanism in detail to understand the role of the synthesis conditions on the properties of polyol-synthesized NMC.

3.3 Polyol synthesis mechanism

3.3.1 Characterization of as-synthesized precipitate

The precursor was prepared as a one-pot synthesis by first dissolving Li^+, Ni^{2+}, Mn^{2+}, and Co^{2+} ions in the polyol solution. After a high-temperature solution reaction at 230 °C, the precipitate obtained is fluffy in nature, implying that the chelating agent has likely formed a complex with the metal ions in the solid precursor [57]. The typical structural and morphological characterizations of the precipitate are shown in Fig. 5. After high-temperature polyol solution reaction, HAADF-STEM images reveal that the precipitate is comprised of crystalline nanoparticles of about 5 nm in diameter, completely dispersed in an amorphous organic matrix. Its local chemical composition was analyzed by STEM-EELS mapping (Fig. 6(a)). The results show that the synthesized nanocrystals are composed of both Ni and Co, while Mn- and O-containing species constitute an amorphous matrix. As the distribution of O was inversely correlated with Ni and Co, it was concluded that in this core/shell-like structure, a Mn-embedded organic "shell" covers a Ni-Co alloy "core". Nanoparticles with only Ni or Co were not observed in other HAADF-STEM images either (Fig. S10 in the ESM). The closely magnified bright-field image and the corresponding fast Fourier transform (FFT) (Fig. 5(c)) verified that Ni-Co alloy nanoparticles are well-crystalline with the observed *d* spacing of 0.20 and 0.17 nm between adjacent fringes, corresponding to the (111) and (200) crystal planes of fcc structured Ni-Co alloy [58–63].

The crystal structure of the precipitate was further analyzed by XRD. The most intense peaks observable on the XRD pattern of the precipitate can be indexed by a face-centered cubic phase (fcc, $Fm\bar{3}m$) with lattice parameter a = 3.530(2) Å as obtained by Le Bail refinement (Fig. 5(a)). The value of the lattice parameter obtained here is intermediate between values typically observed for pure Ni metal ($a \approx 3.52$ Å) and Co metal ($a \approx 3.54$ Å), suggesting that Ni and Co form an alloy (Table S5 in the ESM). Note that Co metal typically stabilizes in hexagonal close-packed (hcp, *P63/mmc*) crystals below 450 °C and in fcc ($Fm\bar{3}m$) crystals above 450 °C. However, the stability of the two phases is heavily influenced by the crystallite size, with smaller crystallite size favoring the fcc polymorph [64], as we observe here. The residual XRD peaks not indexed by the fcc phase cannot be properly refined by an additional hcp phase, although a hcp phase with lattice parameters a = 2.659 Å and c = 4.354 Å yields peaks close to those observed experimentally (Fig. S11 in the ESM). This discrepancy suggest the presence of disorder (e.g. stacking faults) in the hcp-like phase which is likely

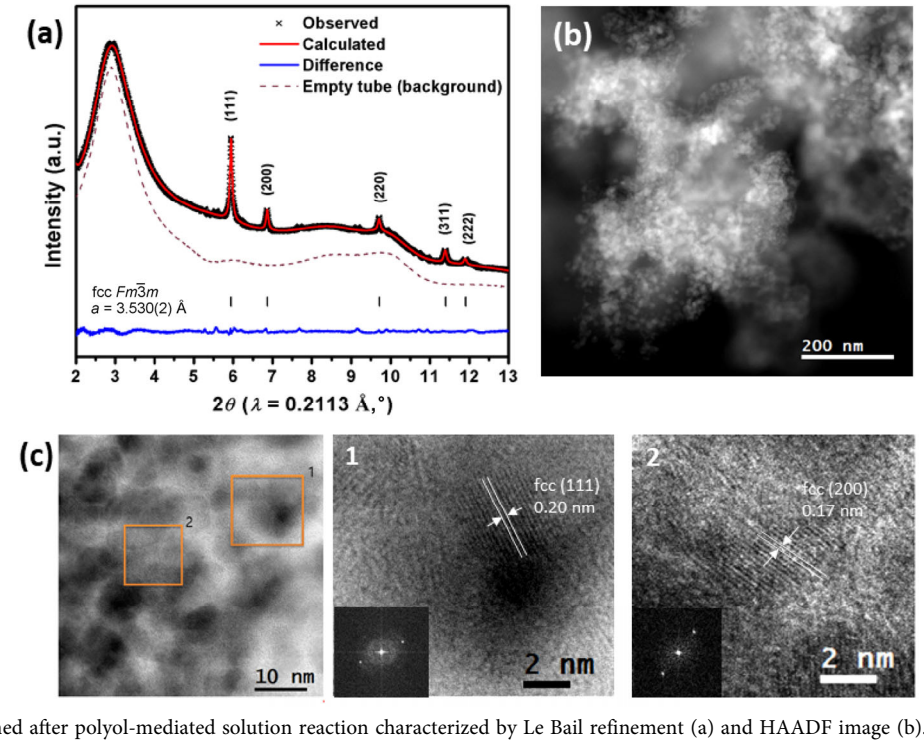

Figure 5 Precipitate obtained after polyol-mediated solution reaction characterized by Le Bail refinement (a) and HAADF image (b). Enlarged bright-field images (c) show crystalline nanoparticles embedded in amorphous matrix.

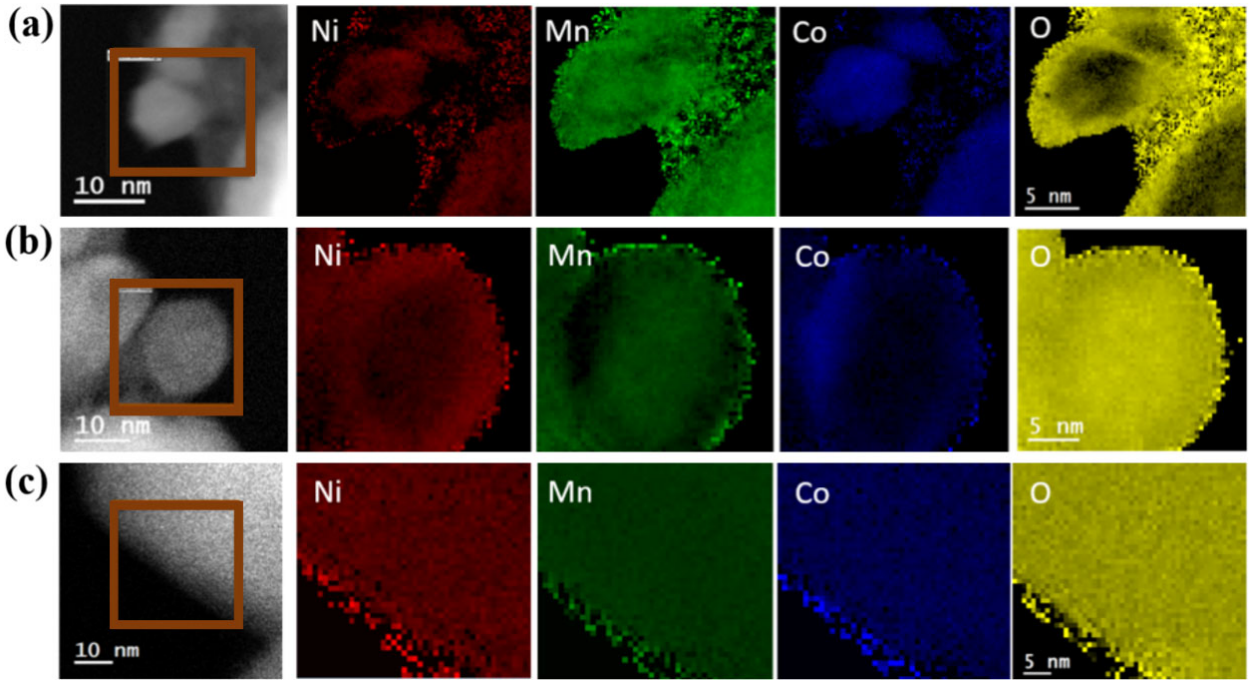

Figure 6 STEM-EELS elemental mapping of as-synthesized precipitate before any heat treatment (a), after 450 °C heat treatment (b), and after 850 °C heat treatment (c).

related to the hcp–fcc intergrowth phenomena previously observed in nanosized Co metal [65, 66].

Single fcc phase refinement of the PDF data in the intermediate range (15–40 Å) seems to be sufficient to fit the PDF data, as the difference (residual) features a sine-like pattern, suggesting that no other phase is present (Fig. S12(a) in the ESM). Crystallite size is estimated to be 7(5) nm, which is consistent with the HAADF-STEM images (Table S6 in the ESM). A two-phase fcc–hcp refinement only marginally improves the quality of the fit, as the R_w decreases from 0.356 to 0.292 (Fig. S12(b) in the ESM). The result of the two-phase fit is characterized by a large standard deviation of the estimated phase fraction—65% and 35% for the fcc and hcp phases, respectively, with a 27% standard deviation. This further supports the presence of a hcp-like phase in the precipitate. The difference at low r displays the contribution of the Mn-rich and organic species to the PDF (Fig. S12(c) in the ESM). With a coherence size of about 7 Å, the amorphous Mn-rich phase features peaks at 1.3, 2.1 Å which are relatively close to those experimentally observed in Mn-acetate tetrahydrate (1.2 and 2.2 Å) [67], which suggests that Mn is not reduced to its metallic form like Ni and Co. We believe that the unique characteristics of the precipitate described above can be ascribed to the distinctive properties of the polyol medium itself. With a high boiling point, the polyol solvent can reduce dissolved metal cations to synthesize a wide variety of metals, intermetallics, and alloys without the need for high pressure conditions [14]. During the reaction, the solvent, triethylene glycol, reduces both Ni^{2+} and Co^{2+}-ions into an alloy, since these metal cations have similar reductivity [68, 69]. On the other hand, Mn^{2+} and Li^{+} keep their original oxidation states and form a precipitate with organic ligands since polyol is not a strong enough reducing agent. The oxidation states of each TM were further verified using sXAS (Fig. 7). Here, we present TEY measurements as fluorescence measurements (TFY and PFY) suffer from self-absorption effects that distort the spectra. From comparison with various TM reference compounds, Ni and Mn oxidation states were determined to be 0 and +2, respectively, based on similar energy positions and spectral features. Although Co is expected to be primarily in the metallic state based on XRD, we find sharp spectral features similar to reference Co^{2+} indicating some Co^{2+} in the precipitate. This lineshape likely reflects mixed 0/+2 oxidation state as the broad metallic lineshape is in the

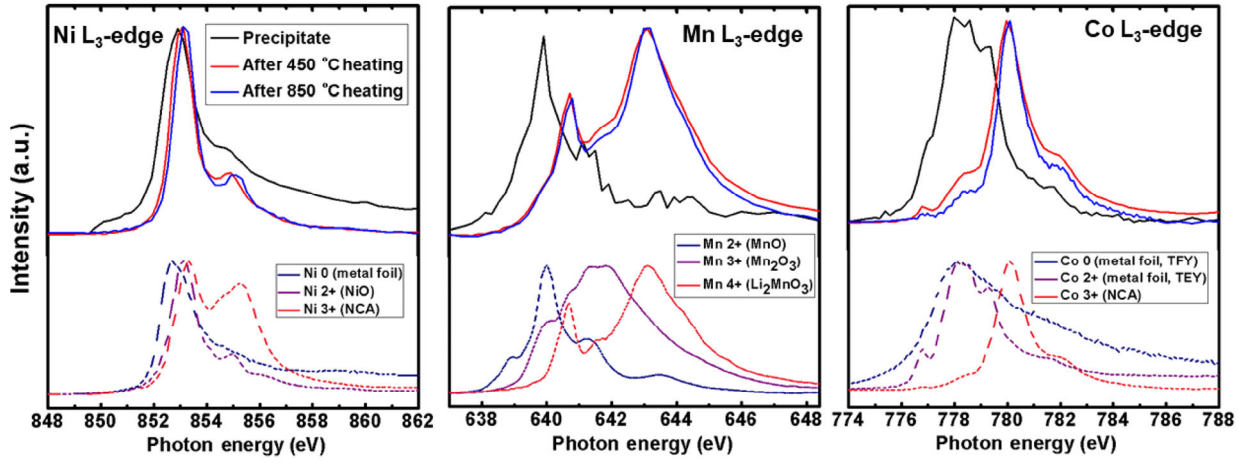

Figure 7 Ni, Mn, and Co L3-edge sXAS spectra of the precipitate, after the first heat treatment at 450 °C, and after the second heat treatment at 850 °C (solid lines) with reference spectra (dash lines).

same energy range as the sharp Co^{2+} peaks [70]. It is possible that not all Co-ions are reduced to the metallic state and that a small extent remained embedded in the organic ligands along with the Mn. Smaller concentrations of Co, compared with Mn, Ni, and O, may pose a challenge in detecting Co-ions in our organic "shell" in the EELS elemental mapping described earlier.

3.3.2 Structural and morphological evolution during the heat-treatment process

After the solution reaction, the obtained precipitate goes through the heat treatment process to form the pure layered phase NMC. Although cathode material synthetic methods can vary widely, a heat treatment is one of the most common and important procedures across all methods. Heat treatment conditions influence important material properties such as phase purity, transition metal distribution, particle size, and defect formation. Herein, *in situ* heating XRD studies were conducted to monitor the structural response of a material with the respect to the temperature.

Figure 8 shows the XRD data recorded during the direct heating of the precipitate. Figure 8(a) represents an image plot of the data recorded in the whole temperature range, while Fig. 8(b) shows selected XRD pattern in the 200–450 °C range, where the most obvious structural changes occur. From room temperature to 220 °C, little changes occur besides thermal expansion of fcc and hcp phases observed in the precipitate. The structural changes start to occur around 230 °C. Figure S13 in the ESM shows the subtraction of the XRD pattern collected at 220 °C from the one obtained at 230 °C to more clearly visualize the low intensity peaks appearing at 230 °C. As shown, this pattern can be indexed by a $CdMn_2O_4$-type spinel phase ($I41/amd$) with lattice parameters a = 5.798(1) and c = 9.038(3) Å. Comparison of these lattice parameters with literature suggests that the spinel phase features a mixed metal composition, such as in $Co_xMn_{3-x}O_4$, rather than the pure-phase Mn_3O_4 analogue [71]. This observation further suggests the presence of Co in the amorphous Mn-rich region.

The spinel phase remains present and acts as an intermediate in the formation of the structurally-related layered phase ($R\bar{3}m$) up to 430 °C. Formation of the layered phase, albeit disordered, is visible from the growth of the (015) peak growing past 270 °C. The reaction of the spinel phase is consistent with the previous temperature dependence oxidation study of Mn- and Co-species [71–74]. Several studies have reported phase transitions from metallic Co nanoparticles to Co_3O_4 and Mn-glycolate to Mn_3O_4 at a similar temperature range. Also, around 270 °C, a noticeable decrease of the diffuse scattering intensity (2θ = 1°–2°) is observed, likely due to the decomposition of organic species from the sample and crystallization of the Li- and Mn-species. This coincides with the appearance of another transient peak when amorphous Li-species crystallize to Li_2CO_3 ($C2/m$) as indicated by the (110) reflection [75, 76]. We expect that in this temperature range, organic species decompose and release Li that react to form Li_2CO_3. At the same time, the metallic alloy grows, as indicated by increase in peak intensity, and then starts to oxidize. Starting from 250 °C, the apparent asymmetry of the (111) reflection of fcc Ni-Co alloy is due to the growth of the (200) reflection of a cubic phase ($Fm\bar{3}m$), likely NiO and/or CoO. Due to the similar electron-density in Ni and Co and the characteristic peak broadness, it is impossible to distinguish between the two. However, as observed in the previous *in situ* studies, we expect that, once formed, CoO would be short-lived and quickly oxidized again to spinel Co_3O_4 phase [74, 77]. In addition, the lattice parameter more closely matches with NiO, therefore, it is more likely that the peaks correspond to NiO. After 420 °C, (110) reflection from Li_2CO_3 also disappears, leaving only NiO and layered NMC structure. In the typical synthesis condition, the material is dwelled at 450 °C for 12 h and then cooled back to room temperature to be thoroughly mixed before starting the higher temperature heat-treatment. NiO rocksalt phase still constitute 9.6(4)% of 450 °C annealed sample, therefore, the second heat-treatment at higher temperature is performed to ensure complete phase transformation to the desired layered NMC.

For the data collected during the second annealing step, Rietveld refinement was employed to diffraction patterns to extract the phase composition and the unit cell parameters as a function of temperature (Table S6 in the ESM). As shown in Fig. S14 in the ESM, the refined cell parameters for both NiO and layered NMC phase mostly follow a linear evolution as a function of annealing temperature. Non-linearity of increase in lattice parameters is observed from 561 to 764 °C which is associated with the material transition from two-phase (NiO and layered oxide) to just a single phase of layered oxide. No new intermediate phase was observed during the second annealing step. As mentioned above, the second annealing process starts with 9.6(4)% NiO and 90(2)% of layered NMC. As the temperature increases beyond the first annealing process, NiO is continuously incorporated into layered NMC and becomes no longer visible in the pattern collected at 764 °C. At the same time, significant narrowing of the peaks and increase in intensity are observed, which can be correlated to a process of crystallite growth. Even after a single phase of layered NMC was achieved, temperature was further increased up to 900 °C and then cooled down to room temperature to reduce the percentage of cation mixing down to 7.38%.

Finally, our study was complemented with *ex situ* STEM-EELS (Fig. 6) and sXAS (Fig. 7) studies. As discussed earlier, prior to heat treatment, the precipitate is composed of Ni-Co alloy nanoparticles wrapped by a Mn- and Li-embedded organic matrix. After the

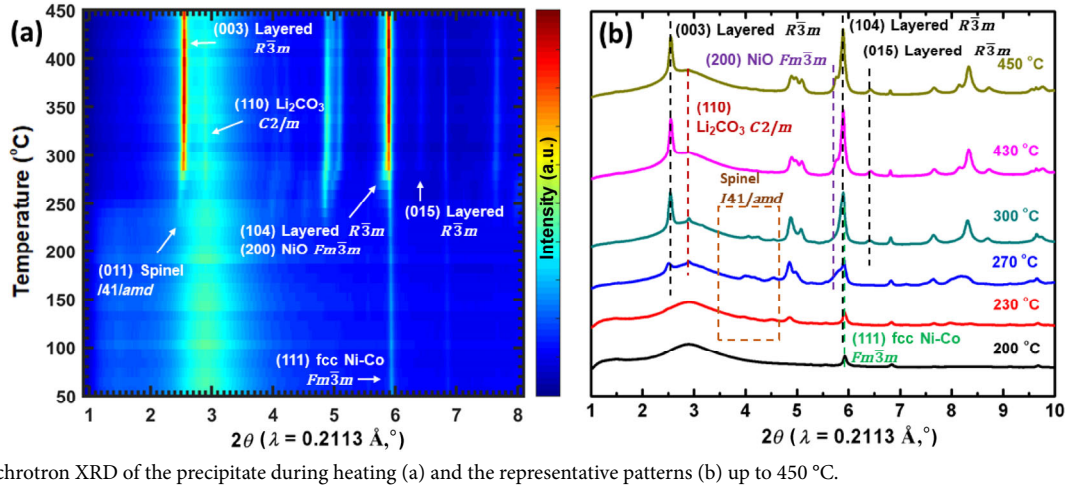

Figure 8 In situ synchrotron XRD of the precipitate during heating (a) and the representative patterns (b) up to 450 °C.

low-temperature heat-treatment at 450 °C, HAADF-STEM images show that the crystal size increased from about 5 to about 20 nm. Amorphous organic species were no longer observed for the sample. All the nanoparticles are crystalline and well-dispersed without any agglomeration. Interestingly, EELS elemental mapping results show that another core/shell-like feature emerged within the particle. As shown, the transition metals are completely oxidized with uniform distribution of oxygen around the particle. However, the transition metals still show obvious chemical segregation with Ni- and Co-rich oxide layer overgrown on a Mn-rich core. We can correlate the elemental segregation of Ni, Co, and Mn with the reaction sequence of the low-temperature heat treatment condition. Mn can form nanocrystals first, due to its proximity to Li in the precipitate form and low reaction temperature. Subsequently, Co from either the Ni-Co alloy and/or organic matrix forms CoO, which quickly transforms into an intermediate spinel phase we observe in XRD. The oxidation state of Co in the spinel would be an approximately +2.7, but further oxidation would shift to +3 as observed in the layered oxide phase. Lastly, the NiO formed from Ni-Co alloy is stable for wide range of temperature, therefore, it persists until the end of the 12-h 450 °C heat treatment. Moreover, Ni and Co also tends to form a "shell" during the oxidation due to Kirkendall effect [74, 78].

After the second heat-treatment, the size of the particles grows to 138 nm but they are still well-dispersed without any agglomeration. STEM-EELS show that all the TM and O are now distributed evenly throughout the sample. sXAS results are also in agreement with XRD results. The oxidation states of TM after the first and the second heat treatment were both confirmed to be +2 for Ni, +3 for Co, and +4 for Mn [79]. Although the 450 °C heat treated sample is still in mixed phase with NiO and the layered NMC, the oxidation state for Ni remains the same for both phases.

In summary, the preceding discussion leads us to propose more detailed reaction schematics as shown in Fig. 9. After all the metal ions are completely dissolved in the polyol solution, Ni^{2+} and Co^{2+} ions get reduced and coalesce as Ni-Co alloy nanoparticles. In the meantime, Li^{+} and Mn^{2+} ions bond with organic ligands and surround Ni-Co alloy in a core/shell-type structure. Then, during the following heat treatment, we observed appearance of the intermediate phases, such as spinel $Co_xMn_{3-x}O_4$ or Li_2CO_3, and transformation to layered oxide phase. On the other hand, the presence of NiO persists through a much larger temperature range and does not fully react until towards the end of the high-temperature treatment. The second heat treatment also results in a decrease of Li/Ni cation mixing and an increase in crystallite size. Similarly, we expect that, during the polyol synthesis of spinel LNMO, Ni^{2+} is reduced Ni^{0} nanometals, while Mn^{2+}-ions precipitate out with organic ligands in amorphous state. As a result, although no crystalline phase in the precipitate is detected due to the low concentration of Ni compared to Mn, 450 °C heat-treated sample is comprised of NiO and spinel phase (Fig. S15 in the ESM). Additional high-temperature heat-treatment is needed to transform NiO into a single spinel phase.

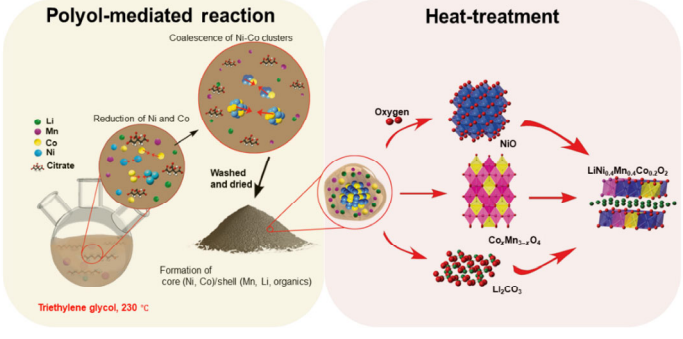

Figure 9 Schematic of the polyol reaction and post heat treatment for layered NMC synthesis.

4 Conclusion

A novel polyol method has been developed to synthesize three cathode materials with different crystal structures. Each product presents uniform elemental and size distribution and exhibits competitive electrochemical performances due to controlled morphology and structural stability. With a dispersive particle morphology, polyol-synthesized cathode materials can also be applied to solid state batteries by providing more intimate contact between solid electrolyte and electrode material. We believe that this method provides a valuable platform for evaluating high-performance, nano-dispersed cathode materials for LIBs. Furthermore, the detailed reaction mechanism has been studied to understand the reaction mechanism underlying each step during the synthesis. Empowered with this knowledge, this novel synthetic method can be employed to develop a wider range of other stable and low-cost intercalation compounds.

Acknowledgements

This work is supported by the NorthEast Center for Chemical Energy Storage (NECCES), an Energy Frontier Research Center funded by the U.S. Department of Energy, Office of Science, Basic Energy Sciences under Award no. DE-SC0012583. The double aberration-corrected scanning TEM (TEAM 0.5) was performed under a proposal to the National Center for Electron Microscopy facility of the Molecular Foundry. Work at the Molecular Foundry was supported by the Office of Science, Office of Basic Energy Sciences, of the U.S. Department of Energy under Contract No. DE-AC02-05CH11231. This research used resources of the Advanced Photon Source, a U.S. Department of Energy (DOE) Office of Science User Facility operated for the DOE Office of Science by Argonne National Laboratory under Contract No. DE- AC02-06CH11357. The work at the ALS was supported by the Office of Basic Energy Sciences, of the U.S. Department of Energy under Contract No. DE-AC02-05CH11231. We also thank beamline scientists Wanli Yang for his assistance with measurements at the ALS iRIXS endstation (Beamline 8.0.1).

Electronic Supplementary Material: Supplementary material (further details on average particle sizes, XRD refinements, ICP-AES data, rate performances, additional HAADF-STEM images and EELS/EDS mappings) is available in the online version of this article at https://doi.org/10.1007/s12274-019-2494-5.

References

[1] Liu, C. F.; Neale, Z. G.; Cao, G. Z. Understanding electrochemical potentials of cathode materials in rechargeable batteries. *Mater. Today* **2016**, *19*, 109–123.

[2] Cho, S. J.; Uddin, M. J.; Alaboina, P. Review of nanotechnology for cathode materials in batteries. In *Emerging Nanotechnologies in Rechargeable Energy Storage Systems: A volume in Micro and Nano Technologies*; Rodriguez-Martinez, L. M.; Omar, N., Eds.; Elsevier Inc.: Amsterdam, 2017.

[3] Armand, M.; Tarascon, J. M. Building better batteries. *Nature* **2008**, *451*, 652–657.

[4] Dunn, B.; Kamath, H.; Tarascon, J. M. Electrical energy storage for the grid: A battery of choices. *Science* **2011**, *334*, 928–935.

[5] Brodd, R. J. *Batteries for Sustainability: Selected Entries from the Encyclopedia of Sustainability Science and Technology*; Springer-Verlag: New York, 2013.

[6] Deshazer, H. D.; La Mantia, F.; Wessells, C.; Huggins, R. A.; Cui, Y. Synthesis of nanoscale lithium-ion battery cathode materials using a porous polymer precursor method. *J. Electrochem. Soc.* **2011**, *158*, A1079–A1082.

[7] Zhang, Z.; Zhu, S. R.; Huang, J. D.; Yan, C. M. Acacia gum-assisted co-precipitating synthesis of $LiNi_{0.5}Co_{0.2}Mn_{0.3}O_2$ cathode material for lithium ion batteries. *Ionics* **2016**, *22*, 621–627.

[8] Zhang, M. H.; Liu, H. D.; Liu, Z.; Fang, C. C.; Meng, Y. S. Modified coprecipitation synthesis of mesostructure-controlled Li-rich layered oxides for minimizing voltage degradation. *ACS Appl. Mater. Interfaces* **2018**, *1*, 3369–3376.

[9] Zhao, R. R.; Yang, Z. L.; Liang, J. X.; Lu, D. L.; Liang, C. C.; Guan, X. C.; Gao, A. M.; Chen, H. Y. Understanding the role of Na-doping on Ni-rich layered oxide $LiNi_{0.5}Co_{0.2}Mn_{0.3}O_2$. *J. Alloys Compd.* **2016**, *689*, 318–325.

[10] Shi, Y.; Zhang, M. H.; Fang, C. C.; Meng, Y. S. Urea-based hydrothermal synthesis of $LiNi_{0.5}Co_{0.2}Mn_{0.3}O_2$ cathode material for Li-ion battery. *J. Power Sources* **2018**, *394*, 114–121.

[11] Zheng, J. M.; Gu, M.; Genc, A.; Xiao, J.; Xu, P. H.; Chen, X. L.; Zhu, Z. H.; Zhao, W. B.; Pullan, L.; Wang, C. M. et al. Mitigating voltage fade in cathode materials by improving the atomic level uniformity of elemental distribution. *Nano Lett.* **2014**, *14*, 2628–2635.

[12] Cao, X.; Zhao, Y.; Zhu, L.; Xie, L.; Cao, X.; Xiong, S.; Wang, C. Synthesis and characterization of $LiNi_{1/3}Co_{1/3}Mn_{1/3}O_2$ as cathode materials for Li-ion batteries via an efficacious sol-gel method. *Int. J. Electrochem. Sci.* **2016**, *11*, 5267–5278.

[13] Fiévet, F.; Lagier, J. P.; Blin, B.; Beaudoin, B.; Figlarz, M. Homogeneous and heterogeneous nucleations in the polyol process for the preparation of micron and submicron size metal particles. *Solid State Ionics* **1989**, *32–33*, 198–205.

[14] Fiévet, F.; Ammar-Merah, S.; Brayner, R.; Chau, F.; Giraud, M.; Mammeri, F.; Peron, J.; Piquemal, J. Y.; Sicard, L.; Viau, G. The polyol process: A unique method for easy access to metal nanoparticles with tailored sizes, shapes and compositions. *Chem. Soc. Rev.* **2018**, *47*, 5187–5233.

[15] Tao, A. R.; Habas, S.; Yang, P. D. Shape control of colloidal metal nanocrystals. *Small* **2008**, *4*, 310–325.

[16] Chupas, P. J.; Chapman, K. W.; Kurtz, C.; Hanson, J. C.; Lee, P. L.; Grey, C. P. A versatile sample-environment cell for non-ambient X-ray scattering experiments. *J. Appl. Cryst.* **2008**, *41*, 822–824.

[17] Toby, B. H.; Von Dreele, R. B. GSAS-II: The genesis of a modern open-source all purpose crystallography software package. *J. Appl. Cryst.* **2013**, *46*, 544–549.

[18] Juhás, P.; Davis, T.; Farrow, C. L.; Billinge, S. J. L. PDFgetX3: A rapid and highly automatable program for processing powder diffraction data into total scattering pair distribution functions. *J. Appl. Cryst.* **2013**, *46*, 560–566.

[19] Farrow, C. L.; Juhas, P.; Liu, J. W.; Bryndin, D.; Božin, E. S.; Bloch, J.; Proffen, T.; Billinge, S. J. L. PDFfit2 and PDFgui: Computer programs for studying nanostructure in crystals. *J. Phys.: Condens. Matter* **2007**, *19*, 335219.

[20] Roisnel, T.; Rodríquez-Carvajal, J. WinPLOTR: A windows tool for powder diffraction pattern analysis. *Mater. Sci. Forum* **2001**, *378–381*, 118–123.

[21] Rodríguez-Carvajal, J. Recent advances in magnetic structure determination by neutron powder diffraction. *Phys. B: Condens. Matter* **1993**, *192*, 55–69.

[22] Qiao, R. M.; Li, Q. H.; Zhuo, Z. Q.; Sallis, S.; Fuchs, O.; Blum, M.; Weinhardt, L.; Heske, C.; Pepper, J.; Jones, M. et al. High-efficiency *in situ* resonant inelastic X-ray scattering (iRIXS) endstation at the advanced light source. *Rev. Sci. Instrum.* **2017**, *88*, 033106.

[23] Li, Q. H.; Qiao, R. M.; Wray, L. A.; Chen, J.; Zhuo, Z. Q.; Chen, Y. X.; Yan, S. S.; Pan, F.; Hussain, Z.; Yang, W. L. Quantitative probe of the transition metal redox in battery electrodes through soft X-ray absorption spectroscopy. *J. Phys. D: Appl. Phys.* **2016**, *49*, 413003.

[24] Dong, H.; Chen, Y. C.; Feldmann, C. Polyol synthesis of nanoparticles: Status and options regarding metals, oxides, chalcogenides, and non-metal elements. *Green Chem.* **2015**, *17*, 4107–4132.

[25] Imamoto, K.; Arai, M. Specific surface area of aggregate and its relation to concrete drying shrinkage. *Mater. Struct.* **2008**, *41*, 323–333.

[26] Capco, D. G.; Chen, Y. S. *Nanomaterial: Impacts on Cell Biology and Medicine*; Springer: New York, 2014.

[27] Zhang, D. R.; Luo, R. Modifying the BET model for accurately determining specific surface area and surface energy components of aggregates. *Constr. Build. Mater.* **2018**, *175*, 653–663.

[28] Tran, N.; Croguennec, L.; Jordy, C.; Biensan, P.; Delmas, C. Influence of the synthesis route on the electrochemical properties of $LiNi_{0.425}Mn_{0.425}Co_{0.15}O_2$. *Solid State Ionics* **2005**, *176*, 1539–1547.

[29] Arrebola, J. C.; Caballero, A.; Cruz, M.; Hernán, L.; Morales, J.; Castellón, E. R. Crystallinity control of a nanostructured $LiNi_{0.5}Mn_{1.5}O_4$ spinel via polymer-assisted synthesis: A method for improving its rate capability and performance in 5 V lithium batteries. *Adv. Funct. Mater.* **2006**, *16*, 1904–1912.

[30] Liu, H.; Zhang, X.; He, X.; Senyshyn, A.; Wilken, A.; Zhou, D.; Fromm, O.; Niehoff, P.; Yan, B.; Li, J. et al. Truncated octahedral high-voltage spinel $LiNi_{0.5}Mn_{1.5}O_4$ cathode materials for lithium ion batteries: Positive influences of Ni/Mn disordering and oxygen vacancies. *J. Electrochem. Soc.* **2018**, *165*, A1886–A1896.

[31] Wang, L. P.; Li, H.; Huang, X. J. Electrochemical properties and interfacial reactions of $LiNi_{0.5}Mn_{1.5}O_{4-\delta}$ nanorods. *Prog. Nat. Sci.: Mater. Int.* **2012**, *22*, 207–212.

[32] Song, J.; Shin, D. W.; Lu, Y. H.; Amos, C. D.; Manthiram, A.; Goodenough, J. B. Role of oxygen vacancies on the performance of $Li[Ni_{0.5-x}Mn_{1.5+x}]O_4$ (x = 0, 0.05, and 0.08) spinel cathodes for lithium-ion batteries. *Chem. Mater.* **2012**, *24*, 3101–3109.

[33] Yang, J. G.; Han, X. P.; Zhang, X. L.; Cheng, F. Y.; Chen, J. Spinel $LiNi_{0.5}Mn_{1.5}O_4$ cathode for rechargeable lithiumion batteries: Nano vs. micro, ordered phase ($P4_332$) vs. disordered phase ($Fd\bar{3}m$). *Nano Res.* **2013**, *6*, 679–687.

[34] Nytén, A.; Thomas, J. O. A neutron powder diffraction study of $LiCo_xFe_{1-x}PO_4$ for x = 0, 0.25, 0.40, 0.60 and 0.75. *Solid State Ionics* **2006**, *177*, 1327–1330.

[35] Bramnik, N. N.; Bramnik, K. G.; Baehtz, C.; Ehrenberg, H. Study of the effect of different synthesis routes on Li extraction–insertion from $LiCoPO_4$. *J. Power Sources* **2005**, *145*, 74–81.

[36] Ludwig, J.; Nilges, T. Recent progress and developments in lithium cobalt phosphate chemistry-syntheses, polymorphism and properties. *J. Power Sources* **2018**, *382*, 101–115.

[37] Mayer, J.; Giannuzzi, L. A.; Kamino, T.; Michael, J. TEM sample preparation and FIB-induced damage. *MRS Bull.* **2007**, *32*, 400–407.

[38] Wolff-Goodrich, S.; Lin, F.; Markus, I. M.; Nordlund, D.; Xin, H. L.; Asta, M.; Doeff, M. M. Tailoring the surface properties of $LiNi_{0.4}Mn_{0.4}Co_{0.2}O_2$ by titanium substitution for improved high voltage cycling performance. *Phys. Chem. Chem. Phys.* **2015**, *17*, 21778–21781.

[39] Zheng, J. M.; Yan, P. F.; Zhang, J. D.; Engelhard, M. H.; Zhu, Z. H.; Polzin, B. J.; Trask, S.; Xiao, J.; Wang, C. M.; Zhang, J. Suppressed oxygen extraction and degradation of $LiNi_xMn_yCo_zO_2$cathodes at high charge cut-off voltages. *Nano Res.* **2017**, *10*, 4221–4231.

[40] Lin, M. X.; Ben, L. B.; Sun, Y.; Wang, H.; Yang, Z. Z.; Gu, L.; Yu, X. Q.; Yang, X. Q.; Zhao, H. F.; Yu, R. C. et al. Insight into the atomic structure of high-voltage spinel $LiNi_{0.5}Mn_{1.5}O_4$ cathode material in the first cycle. *Chem. Mater.* **2015**, *27*, 292–303.

[41] Ben, L. B.; Yu, H. L.; Chen, B.; Chen, Y. Y.; Gong, Y.; Yang, X. N.; Gu, L.; Huang, X. J. Unusual spinel-to-layered transformation in $LiMn_2O_4$ cathode explained by electrochemical and thermal stability investigation. *ACS Appl. Mater. Interfaces* **2017**, *9*, 35463–35475.

[42] Huang, R.; Ikuhara, Y. STEM characterization for lithium-ion battery cathode materials. *Curr. Opin. Solid State Mater. Sci.* **2012**, *16*, 31–38.

[43] Gu, M.; Belharouak, I.; Genc, A.; Wang, Z. G.; Wang, D. P.; Amine, K.; Gao, F.; Zhou, G. W.; Thevuthasan, S.; Baer, D. R. et al. Conflicting roles of nickel in controlling cathode performance in lithium ion batteries. *Nano Lett.* **2012**, *12*, 5186–5191.

[44] Armstrong, R. A.; Holzapfel, M.; Novak, P.; Johnson, C. S.; Kang, S. H.; Thackeray, M. M.; Bruce, P. G. Demonstrating oxygen loss and associated structural reorganization in the lithium battery cathode $Li[Ni_{0.2}Li_{0.2}Mn_{0.6}]O_2$. *J. Am. Chem. Soc.* **2006**, *128*, 8694–8698.

[45] Ryu, W. H.; Lim, S. J.; Kim, W. K.; Kwon, H. 3-D dumbbell-like $LiNi_{1/3}Mn_{1/3}Co_{1/3}O_2$ cathode materials assembled with nano-building blocks for lithium-ion batteries. *J. Power Sources* **2014**, *257*, 186–191.

[46] Xiao, J.; Chen, X. L.; Sushko, P. V.; Sushko, M. L.; Kovarik, L.; Feng, J. J.; Deng, Z. Q.; Zheng, J. M.; Graff, G. L.; Nie, Z. M. et al. High-performance $LiNi_{0.5}Mn_{1.5}O_4$ Spinel controlled by Mn^{3+} concentration and site disorder. *Adv. Mater.* **2012**, *24*, 2109–2116.

[47] Wu, Q.; Zhang, X. P.; Sun, S. W.; Wan, N.; Pan, D.; Bai, Y.; Zhu, H. Y.; Hu, Y. S.; Dai, S. Improved electrochemical performance of spinel $LiMn_{1.5}Ni_{0.5}O_4$ through MgF_2 nano-coating. *Nanoscale* **2015**, *7*, 15609–15617.

[48] Bramnik, N. N.; Nikolowski, K.; Baehtz, G.; Bramnik, K. G.; Ehrenberg, H. Phase transitions occurring upon lithium insertion-extraction of $LiCoPO_4$. *Chem. Mater.* **2007**, *19*, 908–915.

[49] Kreder III, K. J.; Assat, G.; Manthiram, A. Microwave-assisted solvothermal synthesis of three polymorphs of $LiCoPO_4$ and their electrochemical properties. *Chem. Mater.* **2015**, *27*, 5543–5549.

[50] Julien, C.; Mauger, A.; Zaghib, K.; Groult, H. Optimization of layered cathode materials for lithium-ion batteries. *Materials* (*Basel*) **2016**, *9*, 595.

[51] Kim, D. H.; Kim, J. Synthesis of $LiFePO_4$ nanoparticles in polyol medium and their electrochemical properties. *Electrochem. Solid-State Lett.* **2006**, *9*, A439–A442.
[52] Chen, Z.; Chao, D. L.; Liu, J. L.; Copley, M.; Lin, J. Y.; Shen, Z. X.; Kim, G. T.; Passerini, S. 1D nanobar-like $LiNi_{0.4}Co_{0.2}Mn_{0.4}O_2$ as a stable cathode material for lithium-ion batteries with superior long-term capacity retention and high rate capability. *J. Mater. Chem. A* **2017**, *5*, 15669–15675.
[53] Lin, F.; Markus, I. M.; Nordlund, D.; Weng, T. C.; Asta, M. D.; Xin, H. L.; Doeff, M. M. Surface reconstruction and chemical evolution of stoichiometric layered cathode materials for lithium-ion batteries. *Nat. Commun.* **2014**, *5*, 3529.
[54] Yoon, W. S.; Balasubramanian, M.; Chung, K. Y.; Yang, X. Q.; McBreen, J.; Grey, C. P.; Fischer, D. A. Investigation of the charge compensation mechanism on the electrochemically Li-ion deintercalated $Li_{1-x}Co_{1/3}Ni_{1/3}Mn_{1/3}O_2$ electrode system by combination of soft and hard X-ray absorption spectroscopy. *J. Am. Chem. Soc.* **2005**, *127*, 17479–17487.
[55] Shkrob, I. A.; Gilbert, J. A.; Phillips, P. J.; Klie, R.; Haasch, R. T.; Bareño, J.; Abraham, D. P. Chemical weathering of layered Ni-rich oxide electrode materials: Evidence for cation exchange. *J. Electrochem. Soc.* **2017**, *164*, A1489–A1498.
[56] Hausbrand, R.; Cherkashinin, G.; Ehrenberg, H.; Gröting, M.; Albe, K.; Hess, C.; Jaegermann, W. Fundamental degradation mechanisms of layered oxide Li-ion battery cathode materials: Methodology, insights and novel approaches. *Mater. Sci. Eng. B* **2015**, *192*, 3–25.
[57] Jiang, X. Y.; Sha, Y. J.; Cai, R.; Shao, Z. P. The solid-state chelation synthesis of $LiNi_{1/3}Co_{1/3}Mn_{1/3}O_2$ as a cathode material for lithium-ion batteries. *J. Mater. Chem. A* **2015**, *3*, 10536–10544.
[58] Helveg, S.; López-Cartes, C.; Sehested, J.; Hansen, P. L.; Clausen, B. S.; Rostrup-nielsen, J. R.; Abild-Pedersen, F.; Nørskov J. K. Atomic-scale imaging of carbon nanofibre. *Nature* **2004**, *427*, 426–429.
[59] Yoon, K. R.; Ko, J. W.; Youn, D. Y.; Park, C. B.; Kim, I. D. Synthesis of Ni-based co-catalyst functionalized W: $BiVO_4$ nanofibers for solar water oxidation. *Green Chem.* **2016**, *18*, 944–950.
[60] Singh, M. K.; Agarwal, A.; Gopal, R.; Swarnkar, R. K.; Kotnala, R. K. Dumbbell shaped nickel nanocrystals synthesized by a laser induced fragmentation method. *J. Mater. Chem.* **2011**, *21*, 11074–11079.
[61] Zhu, J. H.; Wei, S. Y.; Li, Y. F.; Pallavkar, S.; Lin, H. F.; Haldolaarachchige, N.; Luo, Z. P.; Young, D. P.; Guo, Z. H. Comprehensive and sustainable recycling of polymer nanocomposites. *J. Mater. Chem.* **2011**, *21*, 16239–16246.
[62] Yao, Q. L.; Chen, X. S.; Lu, Z. H. Catalytic dehydrogenation of NH_3BH_3, N_2H_4, and $N_2H_4BH_3$ for chemical hydrogen storage. *Energy Environ. Focus* **2014**, *3*, 236–245.
[63] Shang, H. S.; Pan, K. C.; Zhang, L.; Zhang, B.; Xiang, X. Enhanced activity of supported Ni catalysts promoted by Pt for rapid reduction of aromatic nitro compounds. *Nanomaterials* **2016**, *6*, 103.
[64] Owen, E. A.; Jones, D. M. Effect of grain size on the crystal structure of cobalt. *Proc. Phys. Soc. B* **1954**, *67*, 456–466.
[65] Li, W.; Borkiewicz, O. J.; Saubanère, M.; Doublet, M. L.; Flahaut, D.; Chupas, P. J.; Chapman, K. W.; Dambournet, D. Atomic structure of 2 nm size metallic cobalt prepared by electrochemical conversion: An *in situ* pair distribution function study. *J. Phys. Chem. C* **2018**, *122*, 23861–23866.
[66] Petit, C.; Wang, Z. L.; Pileni, M. P. Seven-nanometer hexagonal close packed cobalt nanocrystals for high-temperature magnetic applications through a novel annealing process. *J. Phys. Chem. B* **2005**, *109*, 15309–15316.
[67] Bertaut, E. F.; Tran Qui, D.; Burlet, P.; Burlet, P.; Thomas, M.; Moreau, J. M. Crystal structure of manganese acetate tetrahydrate. *Acta Cryst.* **1974**, *B30*, 2234–2236.
[68] Luna, C.; del Puerto Morales, M.; Serna, C. J.; Vázquez, M. Multidomain to single-domain transition for uniform $Co_{80}Ni_{20}$ nanoparticles. *Nanotechnology* **2003**, *14*, 268–272.
[69] Sanz, R.; Luna, C.; Hernández-Vélez, M.; Vázquez, M.; López, D.; Mijangos, C. A magnetopolymeric nanocomposite: $Co_{80}Ni_{20}$ nanoparticles in a PVC matrix. *Nanotechnology* **2005**, *16*, 278–281.
[70] Regan, T. J.; Ohldag, H.; Stamm, C.; Nolting, F.; Lüning, J.; Stöhr, J.; White, R. L. Chemical effects at metal/oxide interfaces studied by X-ray-absorption spectroscopy. *Phys. Rev. B* **2001**, *64*, 214422.
[71] Hu, L.; Zhong, H.; Zheng, X. R.; Huang, Y. M.; Zhang, P.; Chen, Q. W. $CoMn_2O_4$ spinel hierarchical microspheres assembled with porous nanosheets as stable anodes for lithium-ion batteries. *Sci. Rep.* **2012**, *2*, 986.
[72] Augustin, M.; Fenske, D.; Bardenhagen, I.; Westphal, A.; Knipper, M.; Plaggenborg, T.; Kolny-Olesiak, J.; Parisi, J. Manganese oxide phases and morphologies: A study on calcination temperature and atmospheric dependence. *Beilstein J. Nanotechnol.* **2015**, *6*, 47–59.
[73] Zhang, D. J.; Jin, C. H.; Li, Z. Y.; Zhang, Z.; Li, J. X. Oxidation behavior of cobalt nanoparticles studied by *in situ* environmental transmission electron microscopy. *Sci. Bull.* **2017**, *62*, 775–778.
[74] Ha, D. H.; Moreau, L. M.; Honrao, S.; Hennig, R. G.; Robinson, R. D. The oxidation of cobalt nanoparticles into Kirkendall-hollowed CoO and Co_3O_4: The diffusion mechanisms and atomic structural transformations. *J. Phys. Chem. C* **2013**, *117*, 14303–14312.
[75] Grenier, A.; Liu, H.; Wiaderek, K. M.; Lebens-Higgins, Z. W.; Borkiewicz, O. J.; Piper, L. F. J.; Chupas, P. J.; Chapman, K. W. Reaction heterogeneity in $LiNi_{0.8}Co_{0.15}Al_{0.05}O_2$ induced by surface layer. *Chem. Mater.* **2017**, *29*, 7345–7352.
[76] Wang, R.; Yu, X. Q.; Bai, J. M.; Li, H.; Huang, X. J.; Chen, L. Q.; Yang, X. Q. Electrochemical decomposition of Li_2CO_3 in NiO-Li_2CO_3 nanocomposite thin film and powder electrodes. *J. Power Sources* **2012**, *218*, 113–118.
[77] Gulbransen, E. A.; Andrew, K. F. The kinetics of the oxidation of cobalt. *J. Electrochem. Soc.* **1951**, *98*, 241–251.
[78] Railsback, J. G.; Johnston-Peck, A. C.; Wang, J. W.; Tracy, J. B. Size-dependent nanoscale kirkendall effect during the oxidation of nickel nanoparticles. *ACS Nano* **2010**, *4*, 1913–1920.
[79] Zhu, J.; Chen, G. Y. Single-crystal based studies for correlating the properties and high-voltage performance of $Li[Ni_xMn_yCo_{1-x-y}]O_2$ cathodes. *J. Mater. Chem. A* **2019**, *7*, 5463–5474.